Supporting Information

Electro-driven multi-functional catalysis separation membrane reactor with wettability switchable for efficient water purification

Mingwei Yuan[a,1], Shiqian Chen[a,1], Bingzheng Zhang[b,1], Jie Liu[a], Shunming Ding[a], Shuhua Wang[a], Weiming Xiao[a], Shunli Shi[a,*], Chao Chen[a,*]

[a] Key Laboratory of Jiangxi Province for Environment and Energy, School of Chemistry and Chemical Engineering, Nanchang University, Nanchang, Jiangxi 330031, P. R. China.

[b] School of Power and Mechanical Engineering, The Institute of Technological Sciences, Wuhan University, Hubei 430072, P. R. China.

*Corresponding author.

E-mail: 1326673354@qq.com (S. Shi), chaochen@ncu.edu.cn (C. Chen).

Characterizations

Surface and cross-section morphologies of the CSMR are observed using a field emission scanning electron microscope (SEM, Hitachi Regulus 8100 and ZEISS Sigma 300). The structural components are characterized by Powder X-ray diffractometer (PXRD, Rigaku Smart Lab 9 kW diffractometer with Cu Kα radiation (λ = 1.541 Å)). FTIR spectra (Nicolet iS10) in a range of 4000-400 cm^{-1}. Thermal gravimetric (TG, Mettler Toledo TGA/DSC 3+ STARe) system with air atmosphere to determine the content of each component. The pore channel and specific surface area were analyzed using Nitrogen adsorption-desorption experiment (Quantachrome, Autosorb iQ2 analyzer, liquid N_2 temperature 77K). All electrochemical measurements were accomplished with a standard three-electrode system on an electrochemical workstation (PARSTAT MC 500, America). X-ray photoelectron spectra (XPS, Thermo Fisher Scientific ESCALAB 25OXi) analyze the valence states of the elements. The hydrophilicity of CSMR is observed using the contact angle (DSA100, KRUSS, Germany). UV-visible spectra (Varian Cary 60, Agilent Technologies Inc, America) are used for concentration detection before and after the catalytic reaction. The Pd content of the samples was measured by inductively coupled plasma-optical emission spectroscopy (Agilent, ICP-OES-5100). In-situ diffused reflectance infrared Fourier transform spectroscopy (in-situ DRIFTs) was undertaken by Nicolet iS10, Thermo Fisher Scientific (U.S.A). The resolution of the iS10 was chosen to be 4 cm^{-1}, and the recording range was from 400 to 4000 cm^{-1}.

DFT simulation

The density functional theory (DFT) calculations is carried out to further comprehend the interactions of various compounds.The simulation process (structure construction, optimization and calculations) is utilizing the Vienna ab initio simulation package (VASP) based on the first-principles[10]. The energy of exchange-correlation is calculated with Perdew-Burke-Ernzerhof (PBE) generalized gradient approximation (GGA)[11-13].The plane-wave basis cut-off energy is obtained at 450 eV. The Gamma k-point grid is performed with 2×2×1[14]. The self-consistent filed tolerance energy is

applied as 10-5 eV. The maxim force tolerance for each atom is below 0.02 eV / Å. The maximum displacement tolerance is derived at 0.005 Å. The interaction between the different materials in contemporary research is established toward the equation of: E_{int} =E_{toal}-$\sum E_{constituent}$ (where E_{toal} and $E_{constituent}$ means the structure optimization energy of the total research system and each constituent in the studying system, correspondingly). A negative E_{int} value indicates that interactions between components can occur spontaneously. Furthermore, higher negative E_{int} represents higher interactions occurring within the system.
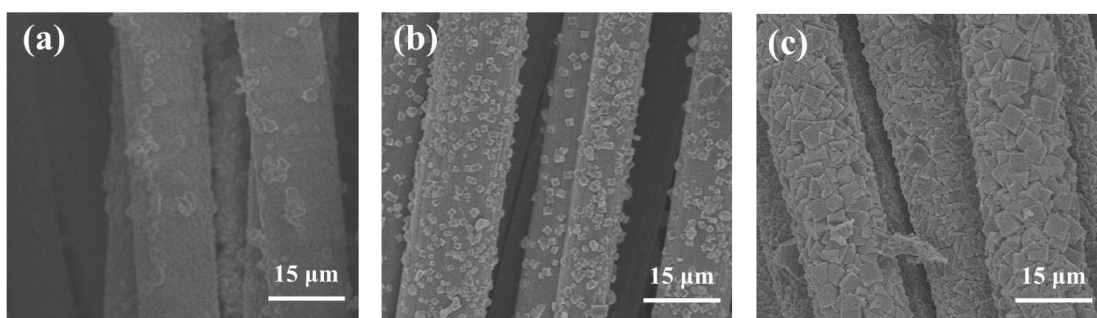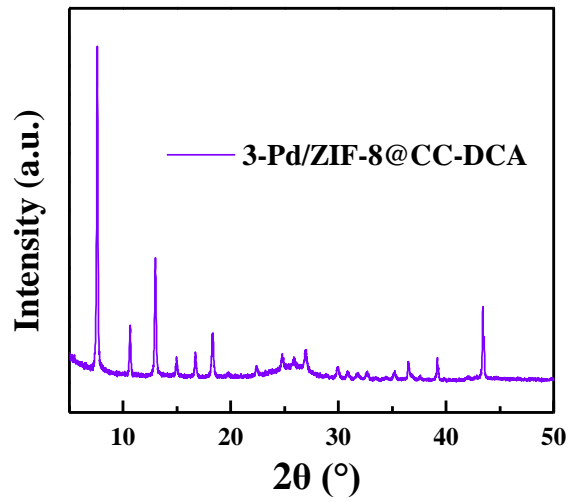
Figure S1. The overall structure SEM images of a) 0.7-ZIF-8@CC-DCA, b) 1-ZIF-8@CC-DCA and c) 2-ZIF-8@CC-DCA, respectively.
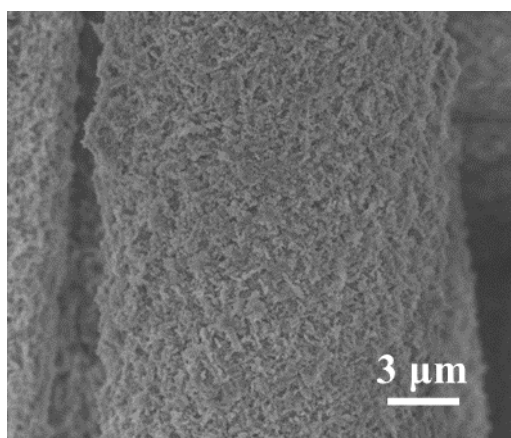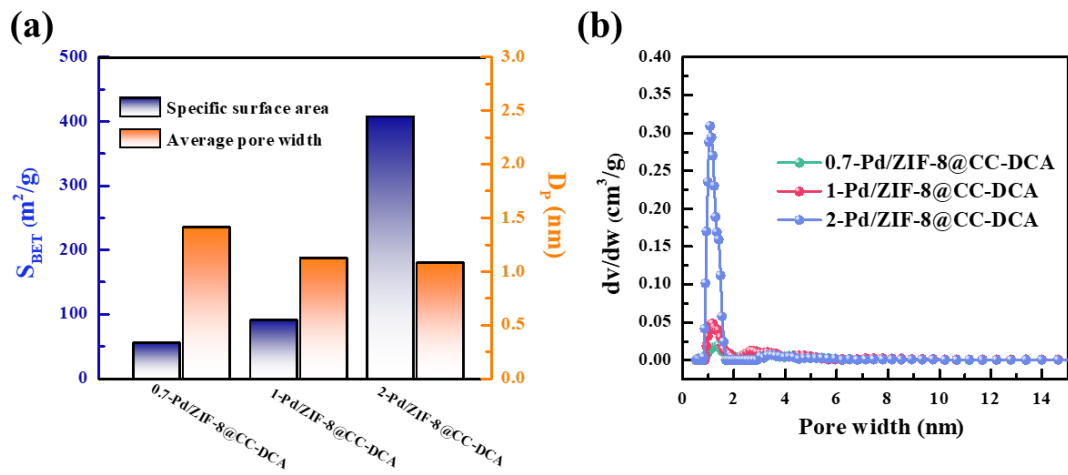

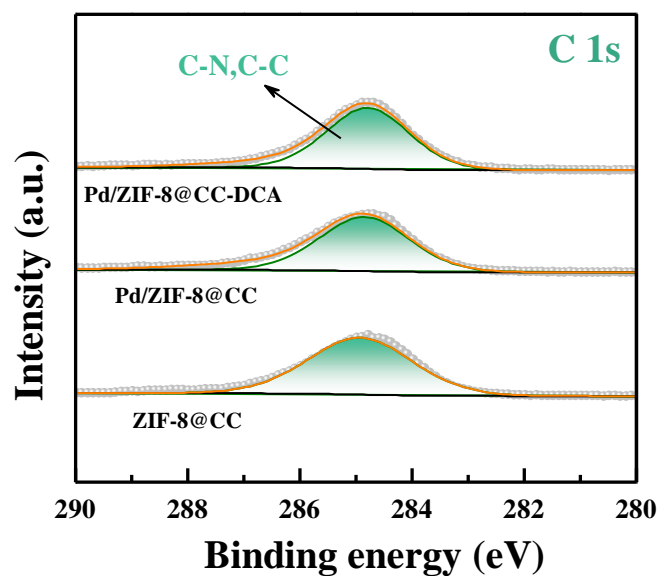**Figure S2.** The SEM image of 3-ZIF-8@CC-DCA.
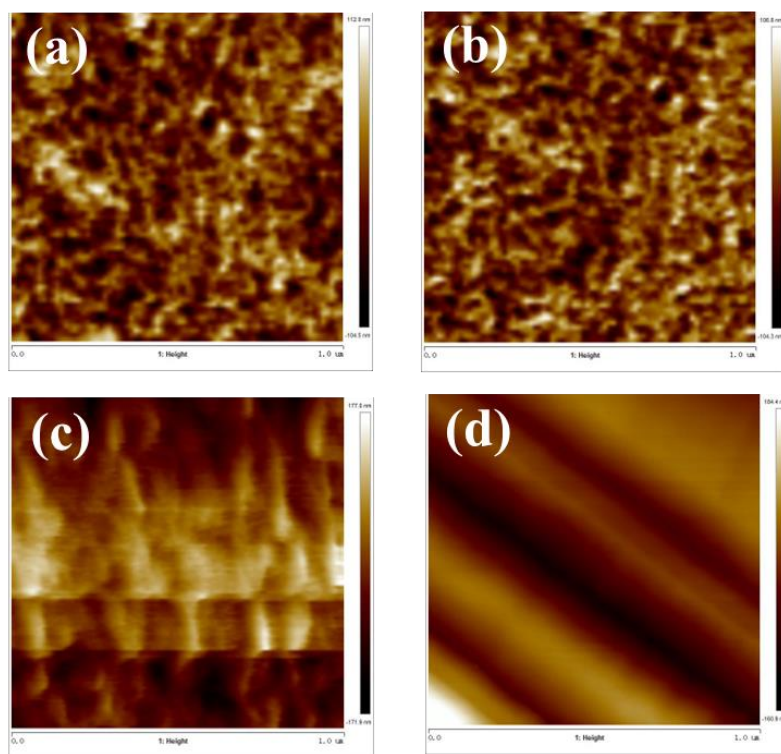
Figure S3. The 2D AFM images of CSMRs of a)pristine carbon cloth, b)0.7-ZIF-8@CC-DCA, c)1-ZIF-8@CC-DCA and d) 2-ZIF-8@CC-DCA, respectively.
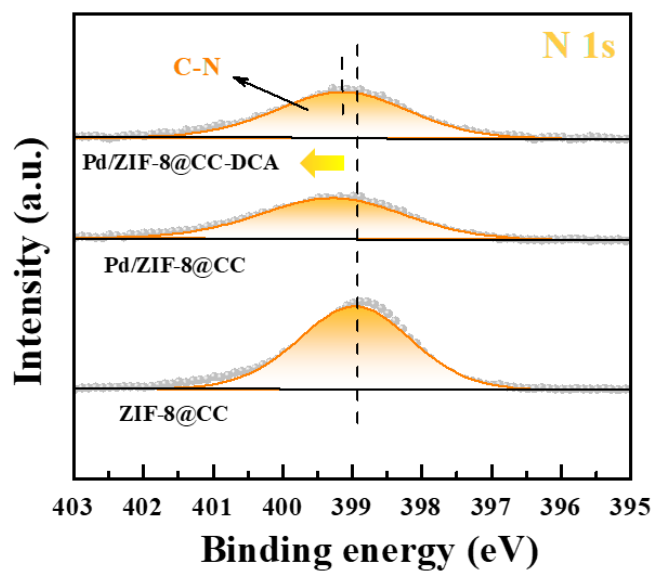
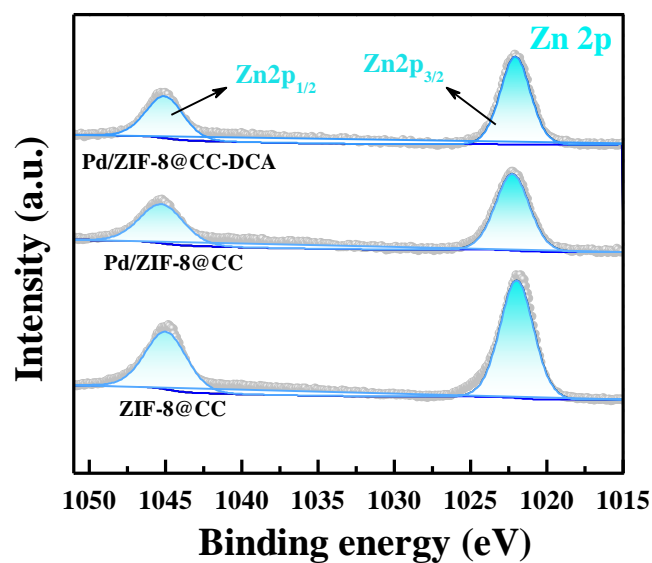**Figure S4.** The XRD pattern of 3-ZIF-8@CC-DCA.

Figure S5. Specific surface and pore size distribution, (b) the aperture distribution NLDFT diagram of 0.7-Pd/ZIF-8@CC-DCA, 1-Pd/ZIF-8@CC-DCA and 2-Pd/ZIF-8@CC-DCA.
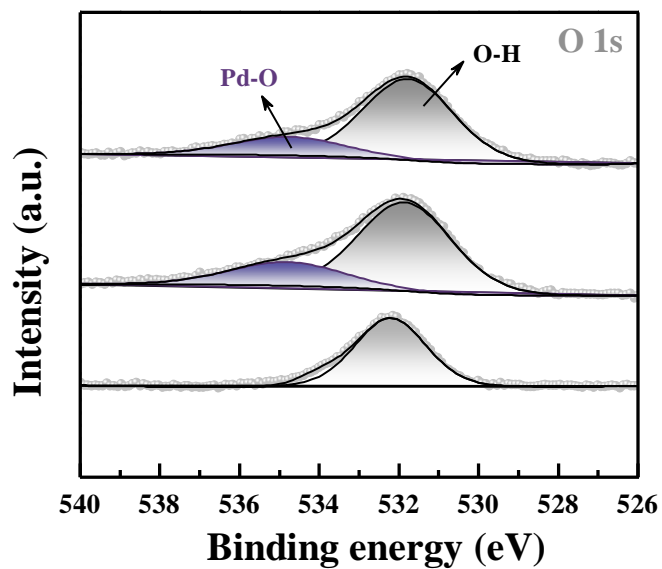
Figure S6. The XPS C 1s core-level spectrum of ZIF-8@CC, Pd/ZIF-8@CC and Pd/ZIF-8@CC-DCA.

Figure S7. The XPS N 1s core-level spectrum of ZIF-8@CC, Pd/ZIF-8@CC and Pd/ZIF-8@CC-DCA.
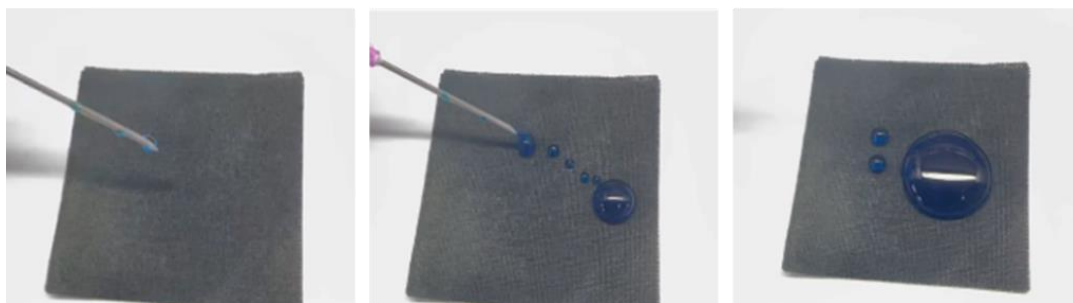
Figure S8. The XPS Zn 2p core-level spectrum of ZIF-8@CC, Pd/ZIF-8@CC and Pd/ZIF-8@CC-DCA.

Figure S9. The XPS O 1s core-level spectrum of ZIF-8@CC, Pd/ZIF-8@CC and Pd/ZIF-8@CC-DCA.
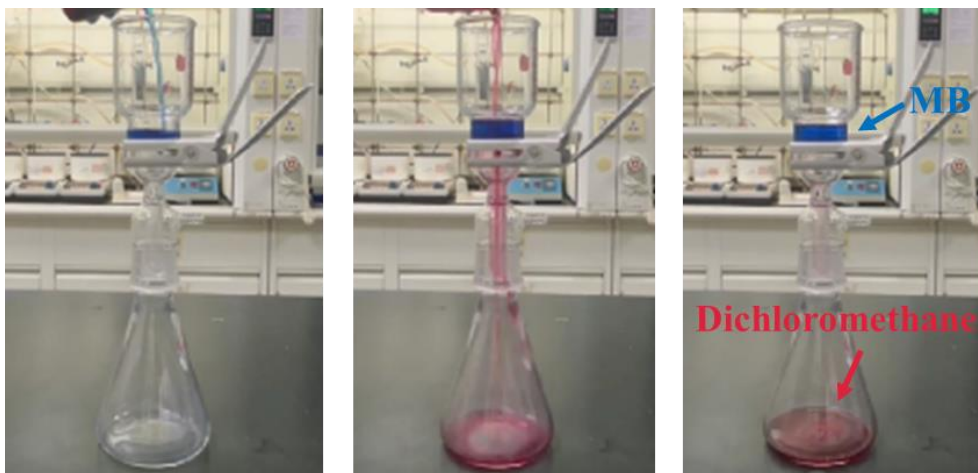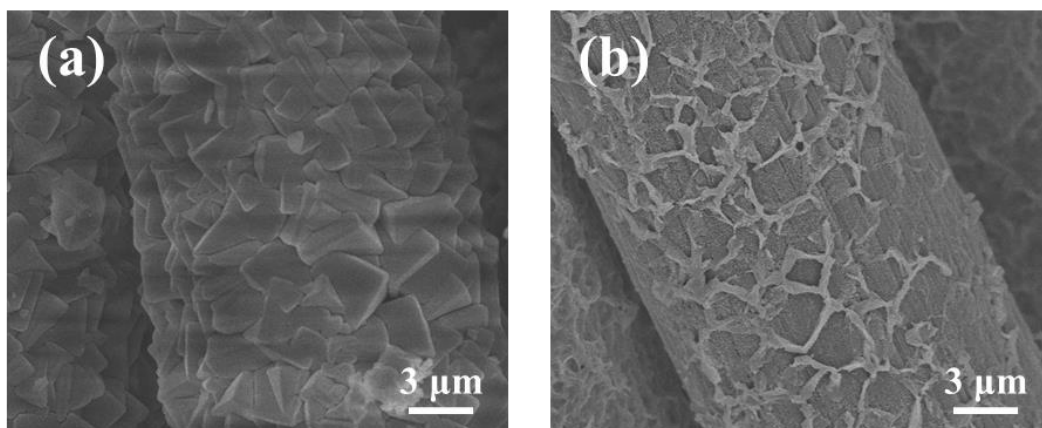
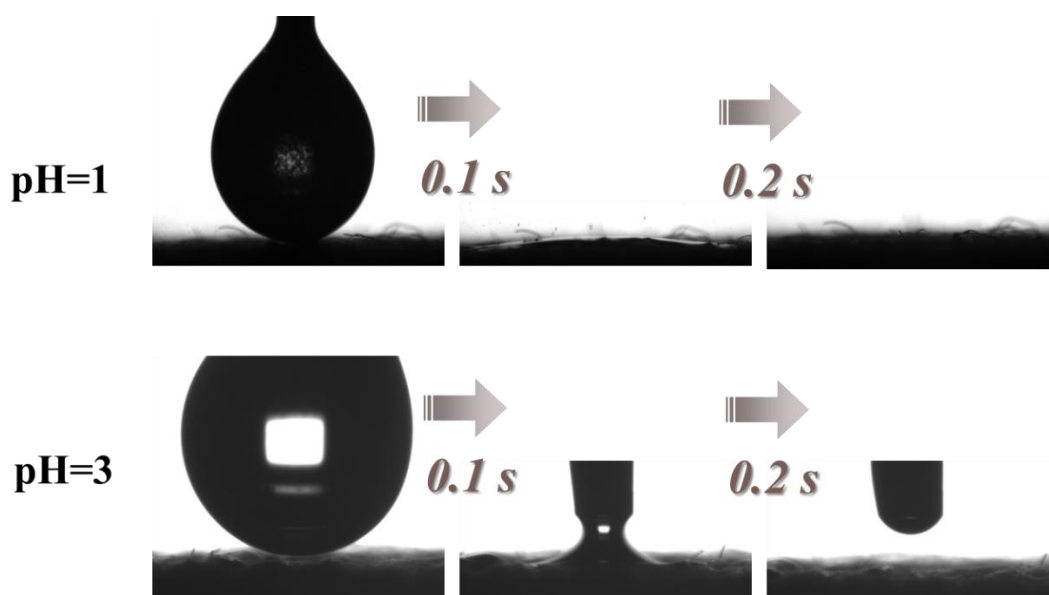**Figure S10**. Strong hydrophobicity of the Pd/ZIF-8@CC-DCA in the air.

Figure S11. Self-cleaning behavior of the Pd/ZIF-8@CC-DCA. The SiO$_2$ particles were completely removed with water droplets rolling off the surface.

Figure S12. The oil/water separation test of MB and dichloromethane.
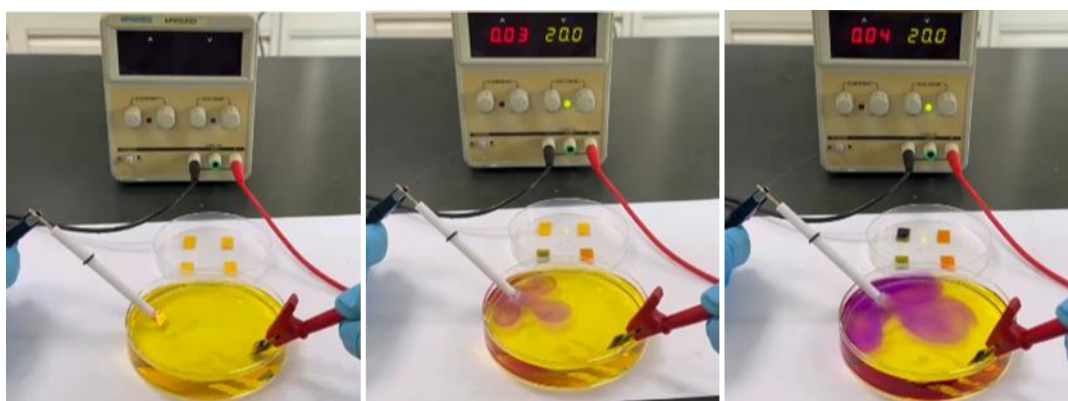

Figure S13. SEM images of Pd/ZIF-8@CC-DCA before (a) and after (b) acid treatment (pH=1).

Figure S14. Photographs of the dynamic shape changes of the water droplets with pH values of (a) 1 and (b) 3 on the Pd/ZIF-8@CC.
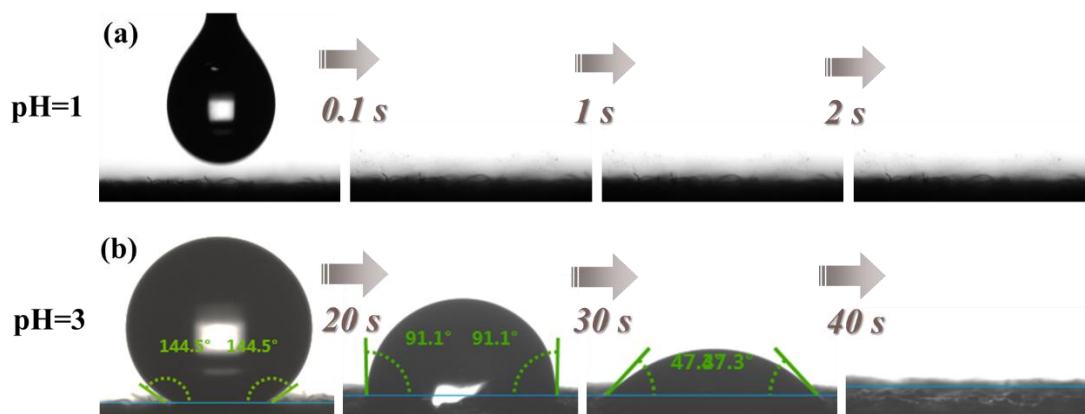
Figure S15. Photographs of the dynamic shape changes of the water droplets with pH values of (a) 1 and (b) 3 on the Pd/ZIF-8@CC-DCA.

Figure S16. Photographs of the experimental setup for pH monitoring during water electrolysis.

Figure S17. The catalytic reaction of MB aqueous solution with 0.1 M Na_2SO_4 was realized by applying voltage switch to change the wettability of Pd/ZIF-8@CC-DCA membrane.
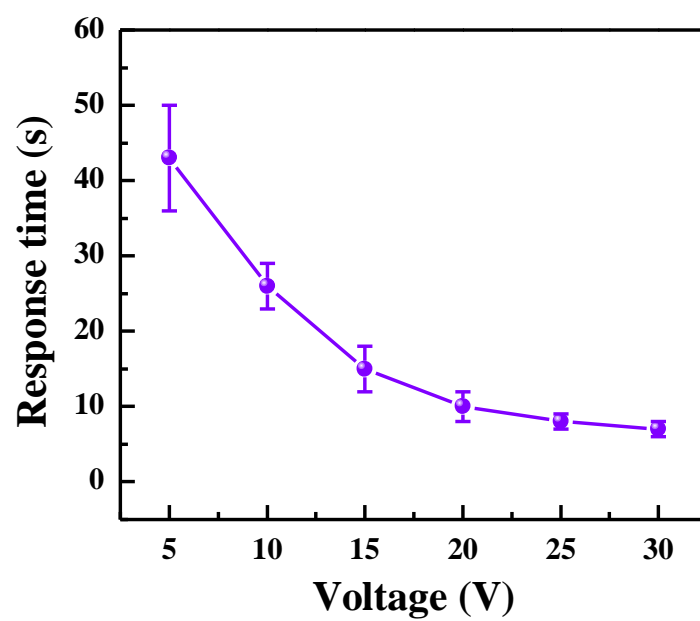
Figure S18. Change of the response time as a function of the applied voltage.
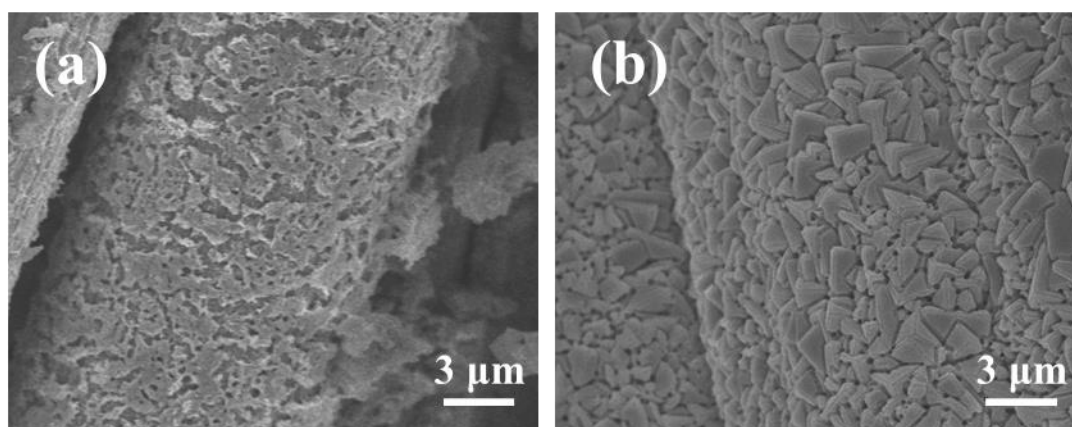
Figure S19. SEM images of Pd/ZIF-8@CC-DCA after (a) acid treatment and (b) electro-treatment.
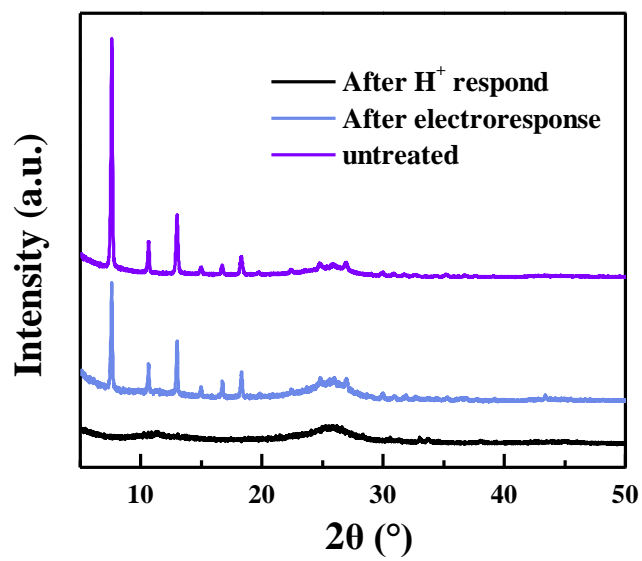
Figure S20. XRD patterns of Pd/ZIF-8@CC-DCA and after HCl treated and after electro-response.
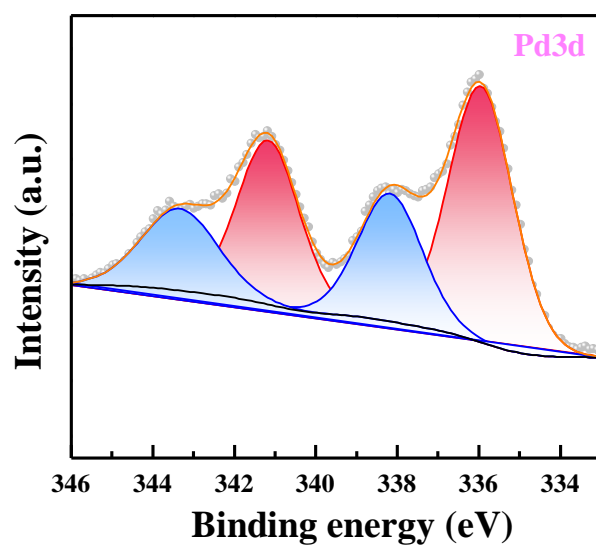
Figure S21. The XPS Pd 3d core-level spectrum of Pd/ZIF-8@CC-DCA after electro-response.

Table S1. ICP test results of Pd content in CSMR

Sample	Theoretical Pd content (wt%)	Actual Pd content (wt%)	Pd content after recycling (wt%)
2-Pd/ZIF-8@CC-DCA	3.0	2.861	2.853
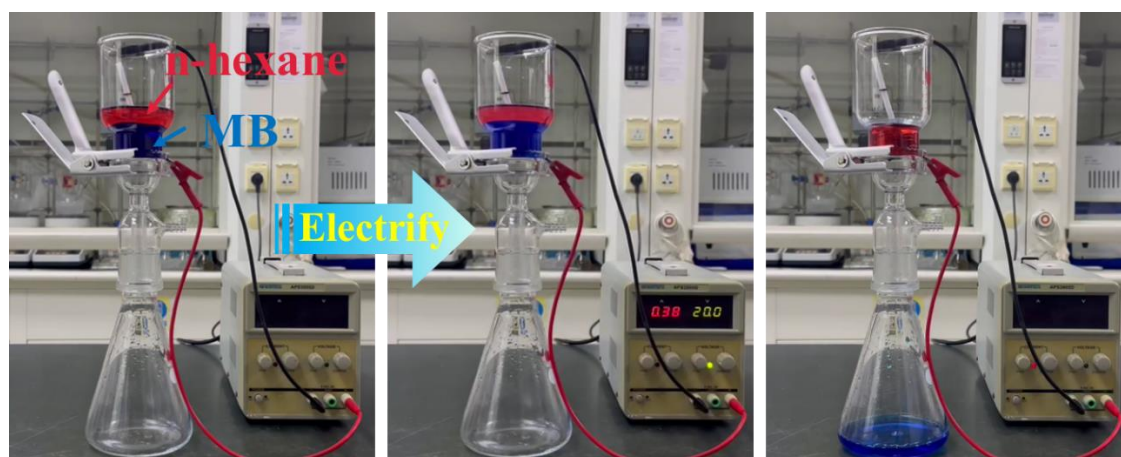
Figure S22. Separation and catalytic process of the n-hexane/MB solution mixture at 20 V. After applying the voltage of 15 V for 10 s, the rejected MB solution passed through the ZIF-8@CC-DCA and there was no fading, the n-hexane was remained.
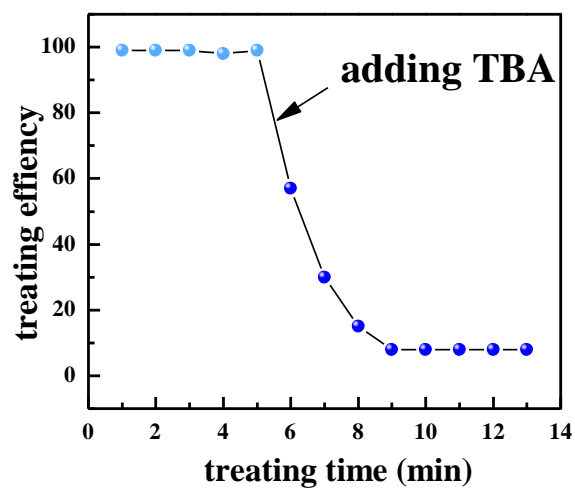
Figure S23. The change of MB degradation efficiency before and after adding hydroxyl radical scavenger ethanol (adding scavenger after 5 minutes of sampling).
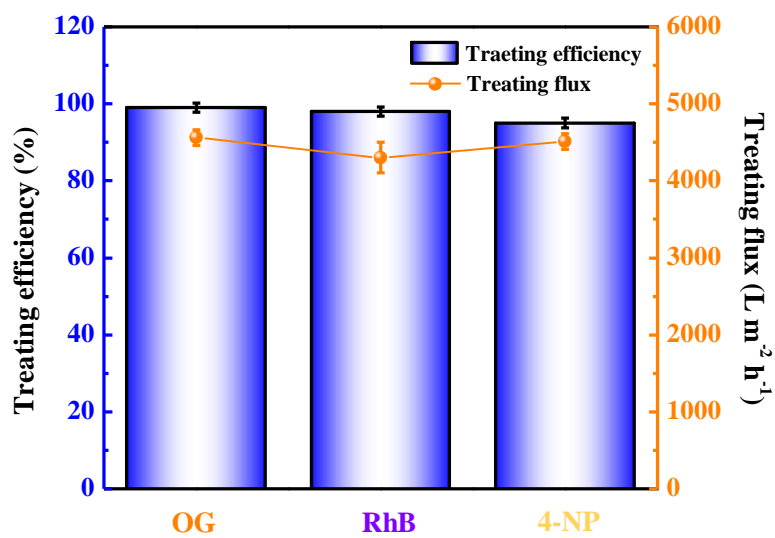
Figure S24. The electrocatalytic degradation efficiency and flux of OG, RhB and 4-NP.

Figure S25. DFT calculations of energy density for dodecylamine molecules a) before and b) after protonation.

Table S2. Comparison between membrane reactor and other wettability responsive functional membrane

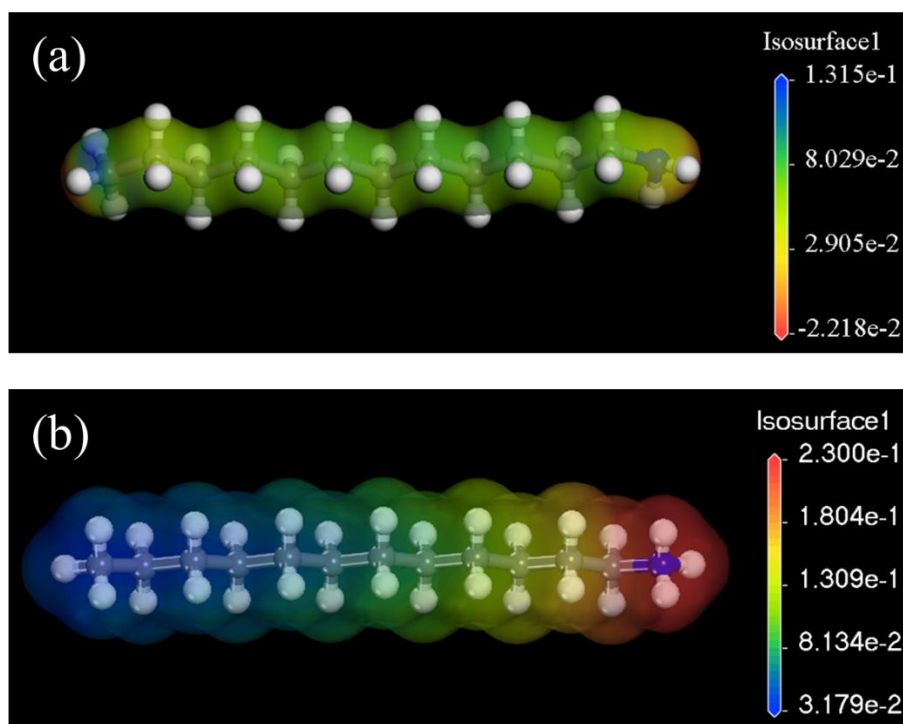| Membrane type	Switching condition	Control method	Response time	Ref.
PVDF/P(AN-co-AM)/P4VP	PH>7	Treat with acidic water	30 s	S1
PVDF-gPAA	pH>6.5	Treat with acidic water	15 s	S2
PVDF-gSiO$_2$ NPs/PAMAM	pH>12	Treat with alkaline water	30 s	S3
PP-SiO$_2$-(PDMAEMA-b-PMMA)	pH<2	Treat with acidic water	20 s	S4
PPy-AOT	electrolyte	Regulating electrode redox potentials	300 s	S5
CAAS-ODA	pH<2	Treated with hydrochloric acid	30 s	S6
E-pH Membrane	Electro responsive	15 V	30 s	S7
PMMA-co-PDEAEMA	CO$_2$ responsive	CO$_2$ and N$_2$	60 min	S8
PNIPAAm/CNT@PVDF	Photo responsive	Infrared light	40 s	S9
Pd/ZIF-8@CC-DCA	Electro responsive	20 V	10 s	This work

References

[1] Y. Ding, S. Xu, H. Zhang, J. Zhang, Z. Qiu, H. Chen, J. Wang, J. Zheng, J. Wu, One-Step Fabrication of a Micro/Nanosphere-Coordinated Dual Stimulus-Responsive Nanofibrous Membrane for Intelligent Antifouling and Ultrahigh Permeability of Viscous Water-in-Oil Emulsions. ACS Appl. Mater. Interfaces 13 (2021) 27635.

[2] B. Cheng, Z. Li, Q. Li, J. Ju, W. Kang, M. Naebe, Development of smart poly(vinylidene fluoride)-graft-poly(acrylic acid) tree-like nanofiber membrane for pH-responsive oil/water separation. J. Membr. Sci. 534 (2017) 1-8.

[3] C. Wei, L. Lin, Y. Zhao, X. Zhang, N. Yang, L. Chen, X. Huang, Fabrication of pH-Sensitive Superhydrophilic/Underwater Superoleophobic Poly(vinylidene fluoride)-graft-(SiO2 Nanoparticles and PAMAM Dendrimers) Membranes for Oil−Water Separation. ACS Appl. Mater. Interfaces 12 (2020) 19130-19139.

[4] T.-T. Li, S. Li, F. Sun, B.-C. Shiu, H.-T. Ren, C.-W. Lou, J.-H. Lin, pH-responsive nonwoven fabric with reversibly wettability for controllable oil-water separation and heavy metal removal. Environ. Res. 215 (2022) 114355.

[5] X. Tan, C. Hu, X. Li, H. Liu, J. Qu, Reversible superwettability switching of a conductive polymer membrane for oil-water separation and self-cleaning. J. Membr. Sci. 605 (2020) 118088.

[6] L. Li, L. Rong, Z. Xu, B. Wang, X. Feng, Z. Mao, H. Xu, J. Yuan, S. Liu, X. Sui, Cellulosic sponges with pH responsive wettability for efficient oil-water separation. Carbohydr. Polym. 237 (2020) 116133.

[7] S. Gan, H. Li, X. Zhu, X. Liu, K. Wei, L. Zhu, B. Wei, X. Luo, J. Zhang, Q. Xue, Constructing Scalable Membrane with Tunable Wettability by Electrolysis-Induced Interface pH for Oil–Water Separation. Adv. Funct. Mater. 33, (2023) 2305975.

[8] Y. Wang, S. Yang, J. Zhang, Z. Chen, B. Zhu, J. Li, S. Liang, Y. Bai, J. Xu, D. Rao, L. Dong, C. Zhang, X. Yang, Scalable and switchable CO_2-responsive membranes with high wettability for separation of various oil/water systems. Nat. Commun. 14 (2023) 1108-1118.

[9] R. Qu, X. Li, W. Zhang, Y. Liu, H. Zhai, Y. Wei, L. Feng, Photothermally induced in situ double emulsion separation by a carbon nanotube/poly(Nisopropylacrylamide)

modified membrane with superwetting properties. J. Mater. Chem. A 8 (2020) 7677-7686.

[10] G. Kresse, J. Furthmüller, Efficiency of ab-initio total energy calculations for metals and semiconductors using a plane-wave basis set. Comput. Mater. Sci. 6 (1996) 15-50;

[11] J. Perdew, K. Burke, M. Ernzerhof, Generalized Gradient Approximation Made Simple. Phys. Rev. Lett. 77(18) (1996) 3865-3868.

[12] P. E. Blöchl, Projector augmented-wave method. Phys. Rev. B 50(24) (1994) 17953-17979.

[13] S. Grimme, Semiempirical GGA-Type Density Functional Constructed with a Long-Range Dispersion Correction. J. Comput. Chem. 27 (2006) 1787-1799.

[14] H. J. Monkhorst, J. D. Pack, Special points for Brillonin-zone integrations. Phys. Rev. B 13(12) (1976) 5188-5192.